Droplet wetting transitions on inclined substrates in the presence of external shear and substrate permeability

Leonardo Espín* and Satish Kumar†
Department of Chemical Engineering and Materials Science, University of Minnesota, Minneapolis, Minnesota 55455, USA
(Received 20 July 2016; published 23 January 2017)

Understanding the gravity-driven motion of droplets on inclined substrates in the presence of external shear and substrate permeability is important for applications such as spray coating and filtration. In this paper, we use a lubrication-theory-based model to study how external shear and substrate permeability affect droplet wetting transitions. A nonlinear evolution equation for the droplet height as a function of time and two spatial variables is derived and numerically solved. The contact-line region is described using a precursor film and disjoining pressure. Depending on its direction, external shear can either suppress or drive wetting transitions, but does not appear to significantly change the critical droplet speeds associated with these transitions. Substrate permeability generally suppresses wetting transitions due to liquid absorption and does appear to significantly affect these critical droplet speeds. The strong influence of substrate permeability and external shear on droplet wetting transitions indicates that it will be important to account for these effects when developing accurate models for industrial applications.

DOI: 10.1103/PhysRevFluids.2.014004

I. INTRODUCTION

The gravity-driven motion of droplets on inclined substrates is one of the most ubiquitous flows in interfacial fluid mechanics, yet it is one of the most challenging to understand. The challenge arises because the flow is generally three-dimensional, is highly nonlinear due to the presence of free surfaces, and has moving contact lines. Experiments on partially wetting droplets have demonstrated that droplets undergo various wetting transitions as droplet speed increases [1,2]. At relatively low speeds, a droplet has a round footprint and attains a terminal shape and velocity. At higher speeds, the rear of a droplet forms an apparent corner, causing the droplet to adopt a teardrop shape. At even higher speeds, a liquid neck forms and breaks up. These transitions can be described, at least qualitatively, using models based on the lubrication approximation [3,4].

The motivation of the present paper comes from the need to understand the influence of external shear and substrate permeability on droplet wetting transitions. This need arises from two different applications, namely spray coating and filtration. In spray coating, droplets impact and then spread on a substrate, which may be inclined and permeable. In addition, external airflows may be present to dry the coating, and these can exert forces on the droplets. In filtration, liquid droplets entrained in air contact and then spread on a fiber mat, which may be inclined and permeable. Here, forces may be exerted on the droplets due to motion of the air. Although both applications involve the presence of multiple droplets that may coalesce, characterizing the behavior of single droplets in an important starting point for building fundamental understanding.

Previous work regarding the influence of external shear on droplet motion has focused on the case in which the substrate is horizontal and impermeable [5], including the case in which droplets are under an air jet [6]. Considerable attention has also been paid to using external shear to move droplets adhered to horizontal substrates (e.g., [7–9]). Experiments have shown how external shear due to

*Present address: Mayo Clinic Neural Engineering Laboratory, Rochester, MN 55905, USA.
†kumar030@umn.edu

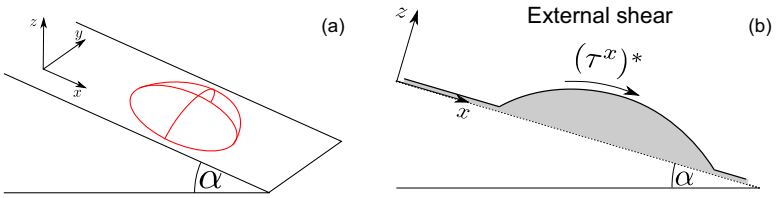

FIG. 1. (a) Schematic of a droplet moving on an inclined substrate. (b) Cross section of the droplet; also shown are a precursor film and a constant external shear stress that acts on the droplet.

airflow can oppose droplet motion on an inclined substrate [10]. Previous work on droplet spreading on permeable substrates has focused on the case in which the substrate is horizontal, and external shear is absent (see Ref. [11] for a recent example). Thus, despite its technological importance, the case of gravity-driven droplet motion on inclined substrates in the presence of external shear and substrate permeability has yet to be treated systematically.

In this paper, we use a lubrication-theory-based model to study droplet wetting transitions on inclined substrates in the presence of external shear and substrate permeability. For the applications mentioned above, the droplets may exhibit non-Newtonian rheology (e.g., [12,13]), and substrate roughness may have a significant influence (e.g., [14]). Nevertheless, we consider here the important limiting case in which the droplet is Newtonian and the substrate is smooth.

The model is presented in Sec. II, and in Sec. III we discuss how to use it to characterize advancing, receding, and equilibrium contact angles. In Sec. IV, droplet wetting transitions in the absence of external shear and substrate permeability are considered, and qualitative comparisons to experimental observations are made. The effects of external shear and substrate permeability are treated in Secs. V and VI, respectively. Finally, concluding remarks are provided in Sec. VII.

II. MATHEMATICAL MODEL

A. Governing equations

We consider a three-dimensional droplet of a Newtonian liquid moving over a permeable substrate located at $z = 0$ and inclined at an angle α with respect to the horizontal (Fig. 1). The droplet flows with velocity (u,v,w), which denote the x, y, and z components of the velocity field, respectively. A constant external shear stress is assumed to act on the droplet. As in prior work [5,15], this shear stress is intended to be a simple model of an external airflow that is parallel to the substrate. We assume that the droplet's characteristic height h^* and radius l^* satisfy $\varepsilon = h^*/l^* \ll 1$, which allows us to apply lubrication theory. A precursor film and two-term disjoining pressure are used to model the behavior of the droplet contact line.

The characteristic speed of the droplet is $u^* = \varepsilon^3\sigma/3\mu$, where σ and μ are the surface tension and viscosity of the liquid, respectively. The corresponding time scale is defined as $t^* = l^*/u^*$, the pressure scale (which can be obtained by balancing the terms from the normal stress balance) as $p^* = h^*\sigma/l^{*2}$, and the disjoining-pressure scale as $\mathscr{A}^* = p^*$. The scale for the external shear is $\tau^* = \sigma h^{*2}/3l^{*3}$, and it can be obtained by balancing the terms in either component of the tangential stress balance. With these scales, we define the following dimensionless variables (denoted with primes):

$$x = l^*x', \quad y = l^*y', \quad z = h^*z',$$
$$u = u^*u', \quad v = u^*v', \quad w = \varepsilon u^*w',$$
$$t = \frac{l^*}{u^*}t', \quad p = p^*p', \quad \Pi = \mathscr{A}^*\Pi',$$

where Π is the disjoining pressure.

At leading order in ε, the equations governing momentum and mass conservation are

$$0 = -p'_{x'} + \tfrac{1}{3}u'_{z'z'} + G_p, \tag{1}$$

$$0 = -p'_{y'} + \tfrac{1}{3}v'_{z'z'}, \tag{2}$$

$$0 = -p'_{z'} - G_n, \tag{3}$$

$$u_{x'} + v_{y'} + w'_{z'} = 0, \tag{4}$$

where $G_p = l^{*3}\rho g \sin(\alpha)/\sigma h^*$ and $G_n = l^{*2}\rho g \cos(\alpha)/\sigma$ are gravitational parameters, ρ is the density of the liquid, and g is the magnitude of the gravitational acceleration. The parameters G_p and G_n characterize the strength of gravitational forces relative to surface-tension forces in the directions parallel and normal to the substrate, respectively.

The air-liquid interface is defined by $z' = h'(x',y',t')$, and the kinematic condition there is

$$h'_{t'} = w' - u'h'_{x'} - v'h'_{y'}. \tag{5}$$

The normal and tangential components of the interfacial stress balance are, at leading order,

$$-p' = h'_{x'x'} + h'_{y'y'} + \Pi', \tag{6}$$

$$u'_{z'} = (\tau^x)', \tag{7}$$

$$v'_{z'} = (\tau^y)', \tag{8}$$

where the dimensionless constants $(\tau^x)' = (\tau^x)^*/\tau^*$ and $(\tau^y)' = (\tau^y)^*/\tau^*$ characterize the strength of the external shear in the x and y directions, respectively. We use a disjoining pressure of the form

$$\Pi' = \mathscr{A}'\left[\left(\frac{b'}{h'}\right)^3 - \left(\frac{b'}{h'}\right)^2\right], \tag{9}$$

which has been used in previous studies of droplet spreading on permeable substrates [11,14,16]. Here, $\mathscr{A}' \geqslant 0$, and the precursor-film thickness is given by $b^* = h^* b'$.

Following Espín and Kumar [11], at the substrate-liquid interface we use the boundary condition

$$w'(x',y',0,t') = -\kappa' p'(x',y',z' = b',t'), \tag{10}$$

which relates liquid absorption by the substrate to the disjoining, hydrostatic, and capillary pressure of the droplet [11]. This condition is complemented with the no-slip condition

$$u'(x',y',0,t') = v'(x',y',0,t') = 0. \tag{11}$$

The imbibition parameter $\kappa' = 3\kappa^* l^{*2}/d^* h^{*3}$ in Eq. (10) controls the rate of liquid absorption. As described in Refs. [11,14], κ^* is the effective permeability of the substrate and d^* is its thickness. For the case of impermeable substrates, $\kappa^* = \kappa' = 0$.

A single evolution equation for the air-liquid interface is obtained by integrating Eqs. (1)–(4) with respect to z, and using boundary conditions (5)–(11). (The procedure is similar to that described in Refs. [15,17].) The evolution equation is (primes dropped)

$$\begin{aligned} h_t = {} & -G_p(h^3)_x + G_n \nabla \cdot (h^3 \nabla h) - \nabla \cdot (h^3 \nabla \nabla^2 h) - \frac{1}{2}(\tau^x, \tau^y) \cdot \nabla h^2 \\ & - \mathscr{A} \nabla \cdot (h^3 \nabla \Pi) - \kappa [G_n(h-b) - \mathscr{A}\Pi - \nabla^2 h]. \end{aligned} \tag{12}$$

B. Solution method

Equation (12) is solved numerically on the domain $0 \leqslant x \leqslant L$, $0 \leqslant y \leqslant P$ subject to the boundary conditions

$$\begin{aligned} h(0,y,t) &= b, \quad h_x(0,y,t) = 0, \\ h(L,y,t) &= b, \quad h_x(L,y,t) = 0, \\ h(x,0,t) &= b, \quad h_y(x,0,t) = 0, \\ h(x,P,t) &= b, \quad h_y(x,P,t) = 0. \end{aligned} \tag{13}$$

Given an initial volume $V_0^* = h^* l^{*2} V_0$, we construct an axisymmetric initial condition. To do this, we define $r = \sqrt{(x-x_0)^2 + (y-y_0)^2}$, where (x_0, y_0) is a point in the computational domain and r_0 determines the droplet edge. For points in the computational domain satisfying $r \leqslant r_0$, the initial condition is given by a fourth-order polynomial $P(r) \equiv h(r, t=0)$, which satisfies symmetry conditions at (x_0, y_0) and the edge conditions

$$P(r_0) = b, \quad P_r(r_0) = 0, \tag{14}$$

together with the volume condition

$$\int_0^{r_0} P(r) dr = V_0 + \pi b r_0^2. \tag{15}$$

Here, the term $\pi b r_0^2$ represents the volume of the precursor film on a disk of radius r_0. For points in the computational domain satisfying $r > r_0$, the initial condition is defined by $h(x,y,0) = b$.

Equation (12), subject to boundary conditions (13), is solved using an alternating direction implicit (ADI) finite-difference scheme similar to that used for higher-order nonlinear diffusion equations [18,19]. A pseudolinear factorization of Eq. (12) is employed, with time-lagged approximations of the nonlinear terms. Second-order centered differences are used to discretize the spatial derivatives, and an iterative procedure is used at each time step to improve the accuracy of the time-lagged approximations. For further details of the numerical scheme, we refer the reader to Refs. [18–21].

In a typical simulation, the domain sizes $L \times P$ range from 5×2 to 15×2.5. Typical discretization sizes vary between 200×200 to 320×240 points per unit area. Given that our ADI code has an ideal structure for running in parallel, we use the OPENMD library to parallelize the code, and typical simulations use between 12 and 32 processors. We note that in cases in which external shear in the y direction is absent ($\tau^y = 0$), our axisymmetric initial condition marched forward in time results in a solution that is symmetric with respect to the plane $y = y_0$. Thus, computation times for this situation can be reduced by halving the computational domain in the y direction and using symmetry boundary conditions at the plane $y = y_0$. A couple of test cases used to validate our code are discussed in the Appendix.

III. ADVANCING, RECEDING, AND EQUILIBRIUM CONTACT ANGLES

If the substrate is horizontal and impermeable, in the absence of external shear the droplet will reach an equilibrium state characterized by an equilibrium contact angle. If the substrate is inclined, the droplet shape can be characterized by advancing and receding contact angles. In this section, we discuss how these angles are determined from our simulations.

The value of the equilibrium contact angle is determined by the values of the disjoining-pressure parameter $\mathscr{A}$ and the precursor-film thickness b [20,21]. In addition, b also controls the terminal droplet speed, with smaller values of b leading to lower speeds. However, smaller values of b lead to a stiffer problem and greater computational costs due to increasing disparity between the precursor-film height and maximum droplet height.

In experimental studies involving droplets moving down inclined planes (in the absence of external shear and substrate permeability), it is observed that the droplets rapidly reach a terminal

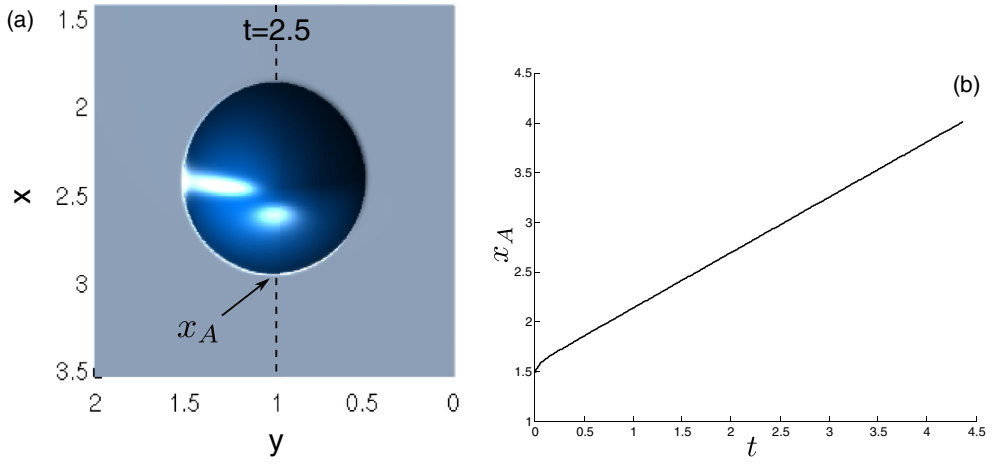

FIG. 2. (a) Terminal shape of a liquid droplet moving down a vertical ($\alpha = 90^\circ$) impermeable substrate in the absence of external shear. (b) Position of the apparent advancing contact line x_A vs time. The parameters used in this simulation are $V_0 = 1, \kappa = 0, G_n = 0, G_p = 10, \tau^x = \tau^y = 0, \mathscr{A} = 4/b$, and $b = 10^{-2}$. The initial condition was centered at $(x_0 = 1, y_0 = 1)$ with $r_0 = 0.25$.

shape and speed when the inclination angle is below a critical value (which depends on droplet volume) [1,2,22]. To confirm that our simulations can capture this behavior qualitatively, we show in Fig. 2 results from simulations of droplet motion on a vertical substrate. The values of $\mathscr{A}$ and b chosen are consistent with those used in prior computational studies [3,4].

Figure 2(a) shows the terminal shape of the droplet. Figure 2(b) shows that this state is attained rapidly, as evidenced by the time evolution of the position of the apparent advancing contact line $x_A(t)$ (defined below), which reaches a constant terminal speed. [In Fig. 2(a) and subsequent images, the color scale is chosen for appearance rather than to convey any quantitative information.]

As noted in Sec. II B, if an initial condition symmetric with respect to a plane $y = y_0$ is used for a simulation, in the absence of lateral external shear ($\tau^y = 0$) the solution will remain symmetric for $t > 0$. In these cases, the solution at the plane of symmetry, $s(x,t) = h(x, y = y_0, t)$, can be used to obtain the apparent advancing (θ_A) and receding (θ_R) contact angles by computing the minimum and maximum slopes of $s(x,t)$, respectively. Similarly, the position of the apparent advancing and receding contact lines, $x_A(t)$ and $x_R(t)$, can be obtained by extrapolating the corresponding tangent lines to the substrate [11]. An example of a computation of x_A is shown in Fig. 2(b), and in Fig. 3 we show the computed advancing and receding angles, superimposed with a plot of $s(x, t = 2.5)$.

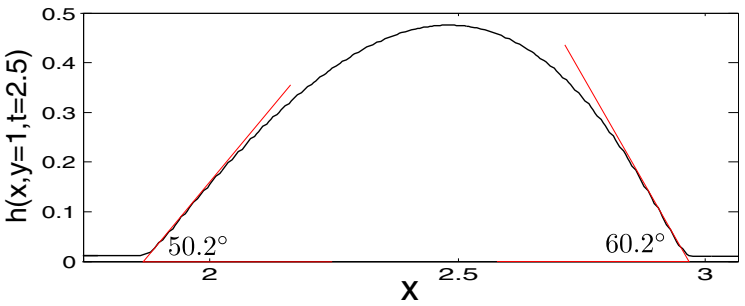

FIG. 3. Cross section of the droplet of Fig. 2(a) at the plane of symmetry $y = 1$, superimposed with the computed terminal advancing and receding contact angles $\theta_A = 60.2^\circ$ and $\theta_R = 50.2^\circ$. For this simulation, the equilibrium contact angle is $\theta_e = 57.3^\circ$.

To determine the equilibrium contact angle, we do a separate simulation on a horizontal substrate. Under these conditions, the solution obtained with our axisymmetric initial condition remains axisymmetric for $t > 0$. This implies that the apparent contact angle along the entire contact line is identical, in which case $\theta_A = \theta_R$. By marching the initial condition forward in time until an equilibrium state is reached [11], we can then define the equilibrium contact angle as $\theta_e = \theta_A$.

This procedure is used to compute θ_e for all the simulations reported in this paper unless stated otherwise. In particular, for the example of Figs. 2 and 3, changing the substrate inclination angle to $\alpha = 0^\circ$ leads to $G_p = 0$ and $G_n = 5.737$. Using these parameters in a simulation, we find that $\theta_e = 57.3^\circ$. For the comparisons with experiments that we carry out in Sec. IV, we fix the value of b and adjust the value of the disjoining-pressure parameter $\mathscr{A}$ until we obtain the value of the equilibrium contact angle reported in the experiments. In matching the values of θ_e from the simulations and experiments, we account for the different scales used in the horizontal and vertical directions [11]. We note that for the lubrication approximation to be strictly valid, θ_e also needs to be small. However, the lubrication approximation often works well far beyond the regime in which it is formally valid (e.g., see Ref. [23]).

IV. ABSENCE OF EXTERNAL SHEAR AND SUBSTRATE PERMEABILITY

To better understand the influence of external shear and substrate permeability, it is useful to first consider what happens when these effects are absent. In this section, we discuss our simulation results for this case and make qualitative comparisons to experimental observations.

A. Wetting transitions

Experiments on droplets moving down inclined planes show that several wetting transitions occur as droplet speed increases. For inclination angles below a critical value (which depends on droplet volume), droplets will attain a terminal speed and a corresponding shape characterized by a round footprint [1,2]. The terminal speed increases with increasing inclination angle, and when the critical value is reached, the droplets develop an apparent corner at their trailing edges, displaying a characteristic teardrop shape [1,2]. At even larger inclination angles, the back of a droplet stretches, forming a liquid neck. The neck eventually breaks up into smaller droplets due to a Plateau-Rayleigh-like instability [1,2], a process referred to as "pearling" [2,3].

To test whether we can reproduce these wetting transitions, we use data taken from Ref. [1], an experimental study of silicone oil droplets moving on a coated glass plate. According to Ref. [1], droplets of 18 μL display all of the wetting transitions described above, which is why we choose to use this volume.

The silicone oil is reported to have viscosity $\mu = 9.15$ cP, surface tension $\sigma = 20.5$ mN/m, density $\rho = 924\,\mathrm{kg/m^3}$, and measured static advancing and receding contact angles of 50° and 40°, respectively [1,4]. From these contact angles, we estimate an equilibrium contact angle of 45° by using the analytical expressions of Tadmor [24], which employ a combination of energetic and geometric arguments to relate θ_A, θ_R, and θ_e. Using a spherical-cap approximation, we estimate a characteristic droplet height of $h^* = 1.23$ mm and radius of $l^* = 2.97$ mm.

For the remainder of this paper, we choose a precursor film thickness $b = 0.005$. For the present case, this represents a dimensional value of $b^* = b \times h^* \approx 6\ \mu$m. Although this is larger than reported values (which range from $\sim$10 nm to $\sim 1\ \mu$m [25]), based on prior studies we do not expect that it will affect the qualitative behavior of our results [5,12]. This value of b allows us to strike a balance between physical realism and computational tractability. Results of limited runs we have performed indicate that reducing the value of b does not change the qualitative behavior of any of our results.

Figure 4 shows droplet shapes at various times obtained from our simulations for three different substrate inclination angles α between 26.3° and 90°. As the inclination angle increases, the droplet goes from having a round footprint to a teardrop shape, with pearling occurring at even higher angles.

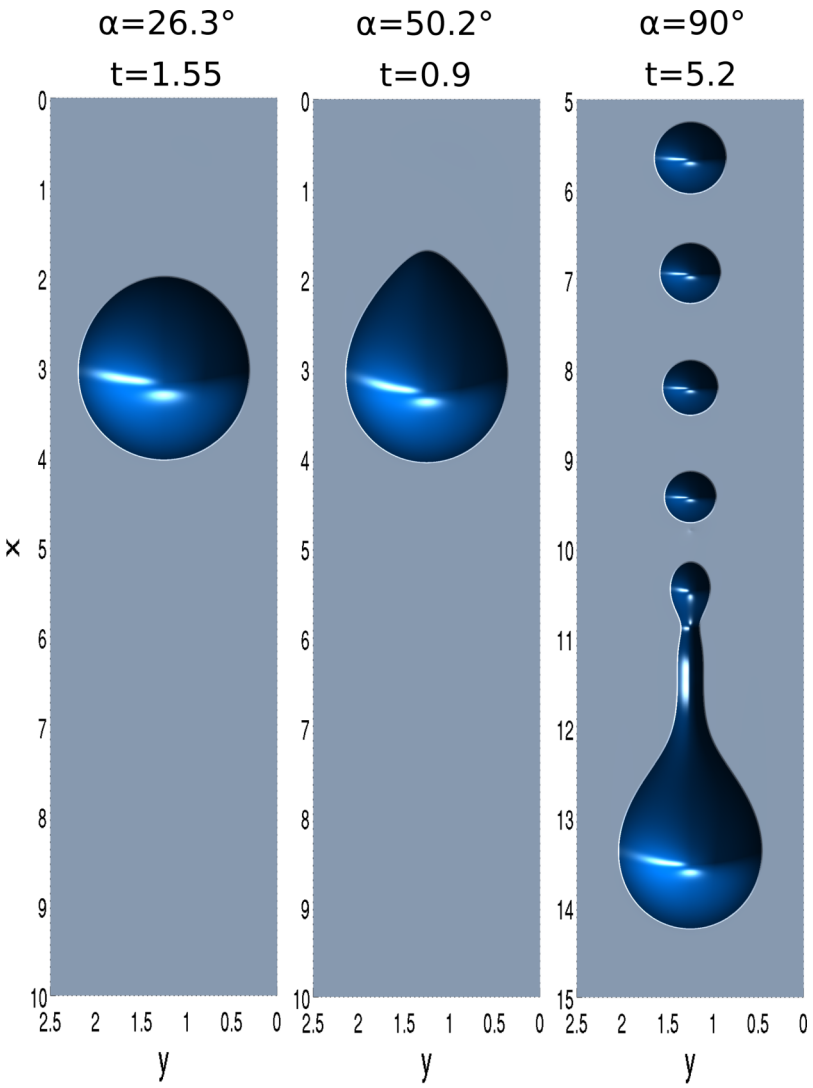

FIG. 4. Wetting transitions for 18 μL droplets moving down substrates with inclination angles α. The parameters used in these simulations are $V_0 = 1.66$, $\kappa = 0$, $\tau^x = \tau^y = 0$, $\mathscr{A} = 7.29/b$ ($\theta_e = 45^\circ$), and $b = 5 \times 10^{-3}$. The gravitational parameters are $G_n = 3.49$, $G_p = 4.16$ ($\alpha = 26.3^\circ$); $G_n = 2.49$, $G_p = 7.23$ ($\alpha = 50.2^\circ$); and $G_n = 0$, $G_p = 9.40$ ($\alpha = 90^\circ$). All quantities shown are dimensionless. The initial conditions were centered at $(x_0 = 1.25, y_0 = 1.25)$ with $r_0 = 0.75$.

Our simulations are thus able to qualitatively capture the wetting transitions that have been observed experimentally as described at the beginning of this section.

Figure 5 shows the positions of the apparent advancing contact lines x_A and the apparent advancing contact angles θ_A corresponding to the simulations of Fig. 4. Figure 5(a) indicates that the droplets rapidly attain a terminal speed, and that larger substrate inclination angles lead to larger terminal speeds. For the droplets on substrates with inclination angles $\alpha = 26.3^\circ$ and 50.2°, terminal shapes are attained at approximately the same time, which can be observed in the behavior of the advancing contact angles, shown in Fig. 5(b).

The unsteady dynamics that occur due to the pearling when $\alpha = 90^\circ$ are reflected in the time evolution of the advancing contact angle. The leading droplet shown in Fig. 4 for $\alpha = 90^\circ$ experiences

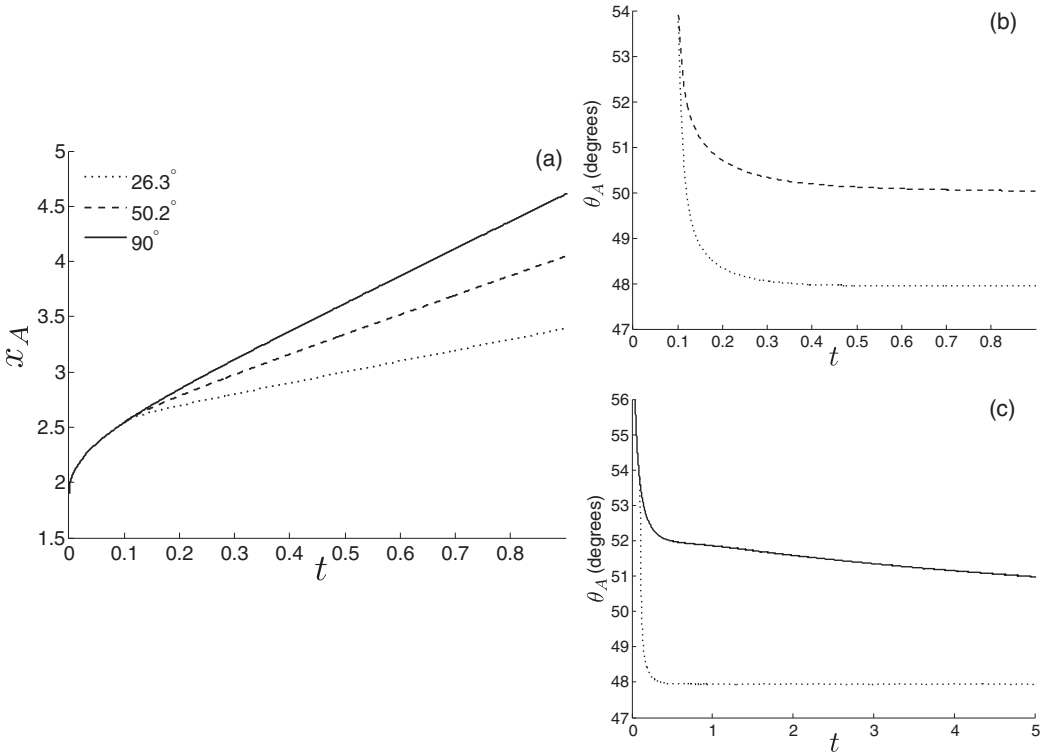

FIG. 5. (a) Time evolution of the apparent advancing contact lines of the droplets of Fig. 4. (b) Time evolution of the apparent advancing contact angles for $\alpha = 26.3^\circ$ and 50.2°. (c) Same as (b) but for $\alpha = 26.3^\circ$ and 90°. All quantities shown are dimensionless. The data for $\alpha = 90^\circ$ are for the leading droplet.

a continuous decrease of height. This is a consequence of the stretching of its rear, which forms a liquid neck that breaks up into smaller droplets, causing the leading droplet to lose mass. This height decrease leads to a continuous decrease of the advancing contact angle of the leading droplet, which is shown in Fig. 5(c). In contrast, the advancing contact angle for a droplet moving on a less inclined substrate ($\alpha = 26.3^\circ$) reaches a constant value.

B. Terminal speeds

We now compare the terminal speeds predicted by our simulations with those observed experimentally. To do this, we perform simulations of $3\,\mu$L droplets. For these droplets, the experimental data we will use [1] correspond to the regime where the droplet has a round footprint. This implies that different substrate inclination angles will only change the terminal speed without causing a wetting transition, making comparisons between simulations and experiments simpler.

Figure 6 shows the experimental data [1] along with our simulation results. Also shown are simulation results from Ref. [4]. The vertical axis is the terminal speed expressed as a capillary number, $\mathrm{Ca} = \mu U/\sigma$, where U is the terminal speed. The horizontal axis is expressed in terms of the inclination angle and Bond number, $\mathrm{Bo} = (V_o^*)^{2/3}\rho g/\sigma$.

As can be seen, our simulations predict that the terminal speed increases linearly with $\sin(\alpha)$, which is qualitatively consistent with the experimental observations. However, the speeds predicted from our simulations with $\theta_e = 45^\circ$ are larger, and they increase more quickly with inclination angle.

We ascribe part of this difference to the relatively large value of b we use, and we would expect the discrepancy to decrease for smaller values of b [3,21,26]. Indeed, the results of Ref. [26] indicate

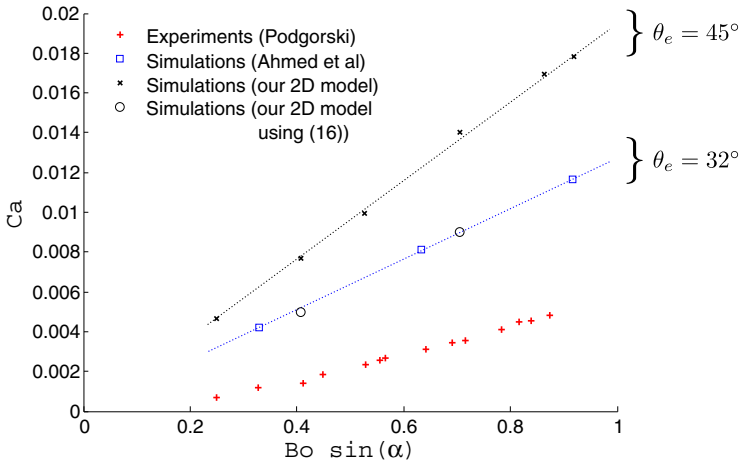

FIG. 6. Terminal droplet speed (Ca) as a function of the substrate angle inclination angle α (and Bo) for 3 μL droplets. The experimental data are from Ref. [1]. The square markers correspond to the highest accuracy simulations of Fig. 10 of Ref. [4]. The parameters used for our simulations are $V_0 = 1.66$, $\tau^x = \tau^y = 0$, and $\kappa = 0$. For $\theta_e = 45°$, we use $\mathscr{A} = 7.29/b$ and $b = 5 \times 10^{-3}$. For $\theta_e = 32°$, we use $\mathscr{A} = 3.42/b$ and $b = 0.01$. The straight lines are linear fits to the simulation data. The initial conditions for our simulations were centered at $(x_0 = 1.25, y_0 = 1.25)$ with $r_0 = 0.75$.

that the predicted speeds come closer to the experimental values for smaller values of b, with the price being a substantial increase in computational costs. Some of the discrepancy may also be due to contact-angle hysteresis [1,2,27,28], which is neglected in our simulations, and the relatively large value of $\theta_e = 45°$, for which the lubrication approximation may be less accurate.

Figure 6 also shows that the terminal speeds predicted from our simulations for $\theta_e = 45°$ are larger than those predicted in Ref. [4]. The simulations of Ref. [4] also yield larger speeds and a faster increase of speed with inclination angle relative to the experiments.

The differences in terminal speeds between our simulations and those of Ref. [4] occur because of differences in how the disjoining-pressure parameter $\mathscr{A}$ (and thus the equilibrium contact angle θ_e) are determined. While we follow the procedure described in Sec. III for determining $\mathscr{A}$, the following expression (obtained from lubrication theory [20,21]) is used in Ref. [4]:

$$\mathscr{A} = \frac{(1 - \cos\theta_e)(n-1)(m-1)}{b\varepsilon^2(n-m)}, \tag{16}$$

where m and n are constants satisfying $n > m > 1$.

By using the values reported in Ref. [4] of $b = 0.01$ and $\theta_e = 45°$ in formula (16), we obtain $\mathscr{A} = 3.42/b$. This value, along with the values of $n = 3$ and $m = 2$, were used in the simulations marked with open circles in Fig. 6. As can be seen, with this choice of parameters, the predictions from our simulations are consistent with those of Ref. [4]. When the above values are used in our simulations to determine θ_e (using the procedure described in Sec. III), we find that θ_e is actually 32° rather than 45°, explaining the differences seen in Fig. 6. We note that the droplet from our simulations with $b = 5 \times 10^{-3}$ and $\theta_e = 45°$ moves faster compared to the droplet from our simulations with $b = 0.01$. Even though the precursor film is thicker in the latter simulations, the droplet moves more slowly because $\theta_e = 32°$ in those simulations. The lower value of θ_e leads to more viscous dissipation [22,29], which slows down the droplet and outweighs the faster terminal speeds that tend to occur at larger values of b.

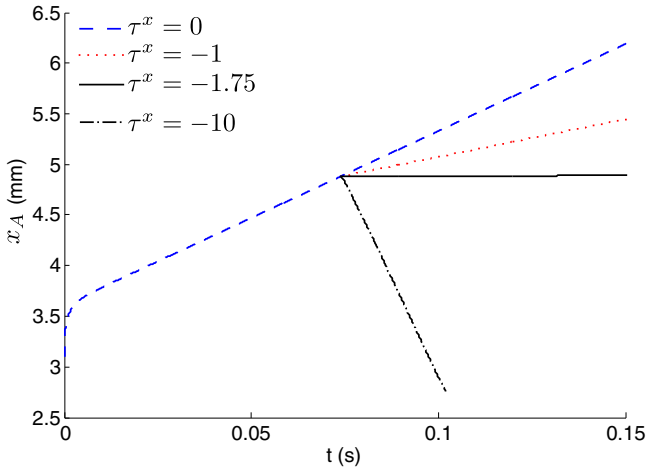

FIG. 7. Positions of the apparent advancing contact lines (in millimeters) vs time (in seconds) for 3 μL droplets moving down a substrate with an inclination angle $\alpha = 26.3^\circ$ in the presence of external shear opposing the downward motion. The parameters used in these simulations are $V_0 = 1.66$, $G_p = 1.26$, $G_n = 1.06$, $\tau^y = 0$, $\kappa = 0$, $\mathscr{A} = 7.29/b$ ($\theta_e = 45^\circ$), and $b = 5 \times 10^{-3}$. External shear is activated impulsively at time $t = 0.07$ s. The initial conditions were centered at $(x_0 = 1.25, y_0 = 1.25)$ with $r_0 = 0.75$.

V. EFFECTS OF EXTERNAL SHEAR ON DROPLET MOTION AND WETTING TRANSITIONS

We now turn to the effects of external shear, considering the case in which the substrate is impermeable. Even when restricting ourselves to the case when lateral shear is absent ($\tau^y = 0$), the effects of external shear are complex, altering the terminal droplet speed and shape, and thus the wetting transitions. External shear can be used to either aid droplet motion ($\tau^x > 0$) or oppose it ($\tau^x < 0$).

We first consider the case in which external shear opposes droplet motion ($\tau^x < 0$; Sec. V A), then we examine the influence of this opposing shear on pearling (Sec. V B), and finally we study the case in which external shear drives wetting transitions ($\tau^x > 0$; Sec. V C). As in Sec. IV, we use simulation parameters motivated by the experiments of Ref. [1].

A. External shear opposing droplet motion

To examine the influence of external shear that opposes droplet motion, we consider the 3 μL droplet of Ref. [1]. For this volume, the droplet has a round footprint and attains a terminal speed in the absence of external shear. We fix the substrate inclination angle at $\alpha = 26.3^\circ$ and vary the strength of the external shear τ^x.

In Fig. 7, we show the effects of opposing external shear on the motion of the 3 μL droplet. For the simulations of Fig. 7, we used as an initial state the solution at time $t = 2.4$ (or $t = 0.07$ s in dimensional time units) of a droplet moving in the absence of external shear (shown with a dashed line in Fig. 7), and marched this initial state forward in time. This is computationally equivalent to starting a simulation at $t = 0$ with the initial condition described in Sec. II B, and using a time-dependent external shear coefficient τ^x, which is zero for $t < 2.4$ and equal to a nonzero value afterward. Thus, the external shear is activated impulsively at a given time.

As shown in Fig. 7, external shear can reduce the terminal speed ($\tau^x = -1$), force the droplet to stop moving ($\tau^x = -1.75$), or even go up the inclined substrate ($\tau^x = -10$). In all the cases shown in this figure, we find that despite the action of external shear, the droplets attain a terminal shape and velocity that are functions of τ^x.

The results of Fig. 7 indicate that for $\tau^x \approx -1.75$, the droplet reaches a steady state as a consequence of external shear balancing the effects of gravity. Furthermore, we find that in this

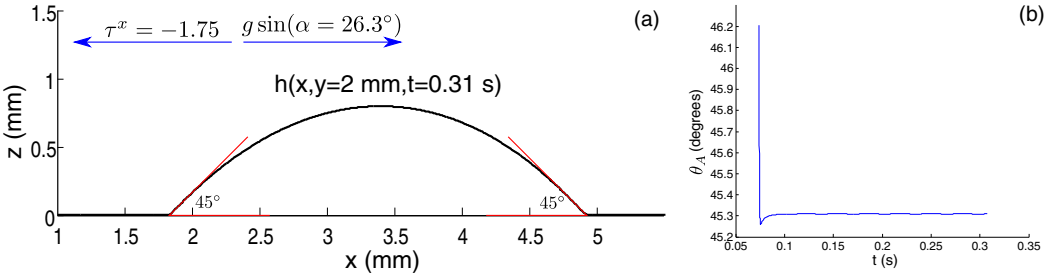

FIG. 8. (a) Cross section at the plane of symmetry $y = y_0$ of the droplet corresponding to the case $\tau^x = -1.75$ of Fig. 7, and (b) time evolution of the apparent advancing contact angle.

steady state the action of surface tension and the disjoining pressure produce a terminal shape that is close to what is observed for a droplet on a horizontal substrate: a spherical-cap shape where the advancing and receding contact angles have reverted back to the equilibrium contact angle $\theta_e = 45^\circ$.

We show this in Fig. 8, where simulation results are presented in dimensional units to give an accurate representation of horizontal and vertical spatial scales. Figure 8(a) shows the cross section at the plane of symmetry of the droplet of Fig. 7 for the case $\tau^x = -1.75$, superimposed with 45° angles. Figure 8(b) shows the time evolution of the apparent advancing contact angle and how it reaches a value close to $\theta_e = 45^\circ$. The correspondence of this steady state with the equilibrium droplet shape on a horizontal substrate is surprising and not at all obvious given the strong nonlinearity and asymmetry of the problem.

In related experimental work, Hashimoto *et al.* [10] used a wind tunnel to produce a uniform air flow opposing the downward motion of water droplets on an inclined substrate. The droplet volumes used in their experiments vary between 10 and 50 μL and the contact angles are large ($102.4^\circ \pm 0.3^\circ$). Despite these differences from our simulation parameters, we can estimate an air speed from our simulations to see if it is comparable to the air speeds used in the experiments, which ranged from 0 to 13 m/s.

To extract an air-speed estimate from our simulations, we relate it to the pressure on the droplet via the following formula [10]:

$$p_{\text{air}} = \tfrac{1}{2} C_p \rho_{\text{air}} V^2, \tag{17}$$

where C_p is a dimensionless drag coefficient that depends on the shape of the object in the air flow, ρ_{air} is the density of air, and V is the air speed. As in Sec. IV A, the characteristic height $h^* = 0.68$ mm and radius $l^* = 1.63$ mm are obtained using a spherical-cap approximation, this time for a 3 μL droplet with a contact angle of 45°. For the computations of Figs. 7 and 8, the external shear scale is $\tau^* = \sigma h^{*2}/3l^{*3} = 0.718$ Pa. As the liquid viscosity is much larger than the air viscosity, we treat the droplet as being rigid and take $C_p = 0.4$ [30]. Then, according to Eq. (17) the air speed corresponding to $\tau^x = 1.75$ is $V \approx 2.4$ m/s, which lies within the range of values used in the experiments.

The above estimate suggests that the effects that we observe in our simulations are physically reasonable. However, we are unaware of experimental data that we can compare directly with our simulations. It should also be noted that our model suggests that a steady state is attained for a single value of the external shear (Fig. 7). However, in Ref. [10], it is reported that downward motion is arrested for a range of air speeds. The large contact angles of the water droplets of Ref. [10] preclude the possibility of a direct comparison with our lubrication-theory-based model. However, we hypothesize that the existence of a range of air speeds for which a steady state is attained is due to contact-angle hysteresis, which is absent from our model.

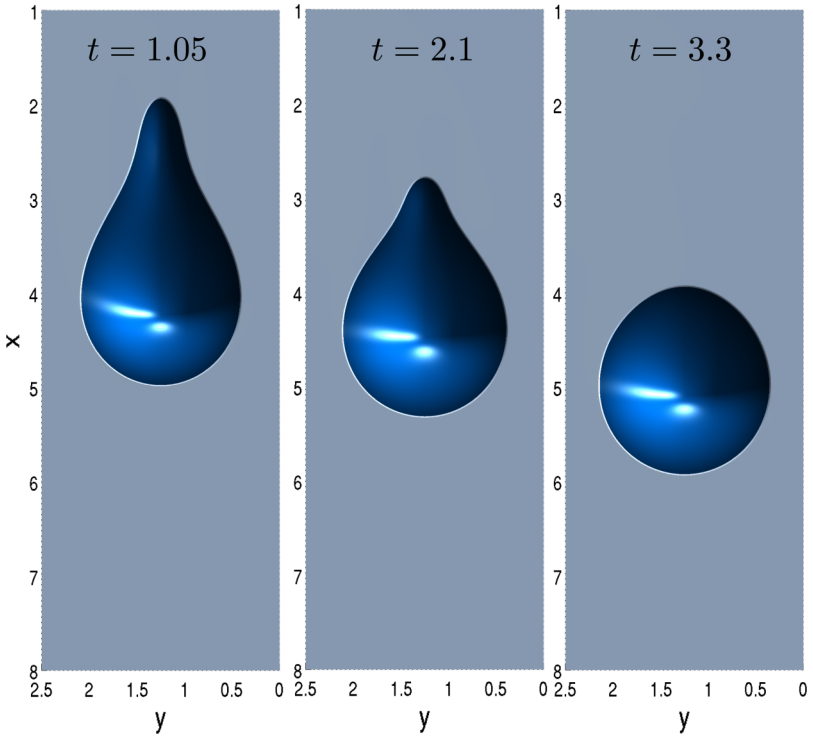

FIG. 9. Pearling process stopped by opposing external shear on an 18 μL droplet moving down a vertical substrate (compare with the $\alpha = 90^\circ$ case of Fig. 4). The parameters used in these simulations are $V_0 = 1.66$, $G_p = 9.40$, $G_n = 0$, $\tau^x = -10$, $\tau^y = 0$, $\kappa = 0$, $\mathscr{A} = 7.29/b$ ($\theta_e = 45^\circ$), and $b = 5 \times 10^{-3}$. External shear is started impulsively at time $t = 1.05$. All quantities shown are dimensionless. The initial droplet shape is the same as that used in Fig. 4.

B. External shear and droplet pearling

The way in which droplet pearling interacts with external shear depends on the state of the droplet at the time the external shear is activated. To illustrate this observation, we focus on the case $\alpha = 90^\circ$ of Fig. 4, where pearling occurs for the 18 μL droplets in the absence of external shear.

Figure 9 shows how opposing external shear can stop the pearling process of an 18 μL droplet moving down a vertical substrate. External shear is started at time $t = 1.05$, reducing the droplet speed and forcing the droplet to revert back to having a round footprint. (The time evolution of the apparent advancing contact line x_A and angle θ_A of this droplet are shown in Fig. 11 with dotted lines.)

We now repeat the calculation of Fig. 9, but we activate the external shear at a later time $t = 2.75$, when the pearling process has already produced a droplet. As shown in Fig. 10, the external shear has a very different effect. Here, external shear slows down the motion of the leading droplet and causes the smaller droplets (pearls) to move upward (as seen from the increasing distance between the pearls and the leading droplet of Fig. 10 as time progresses). In addition, the external shear stops the stretching of the liquid neck on the main droplet. The number and size of the liquid pearls is also reduced compared to the $\alpha = 90^\circ$ case of Fig. 4, where pearling occurs in the absence of external shear ($\tau^x = 0$).

In Fig. 11(a), we show the positions of the apparent advancing contact lines x_A of the droplet of Fig. 9, the leading droplet of Fig. 10, and the leading droplet of the $\alpha = 90^\circ$ case of Fig. 4. This figure shows how the impulsive activation of the external shear alters the motion of a droplet, reducing its speed. In Fig. 11(b), we show the time evolution of the apparent advancing contact angles θ_A of the

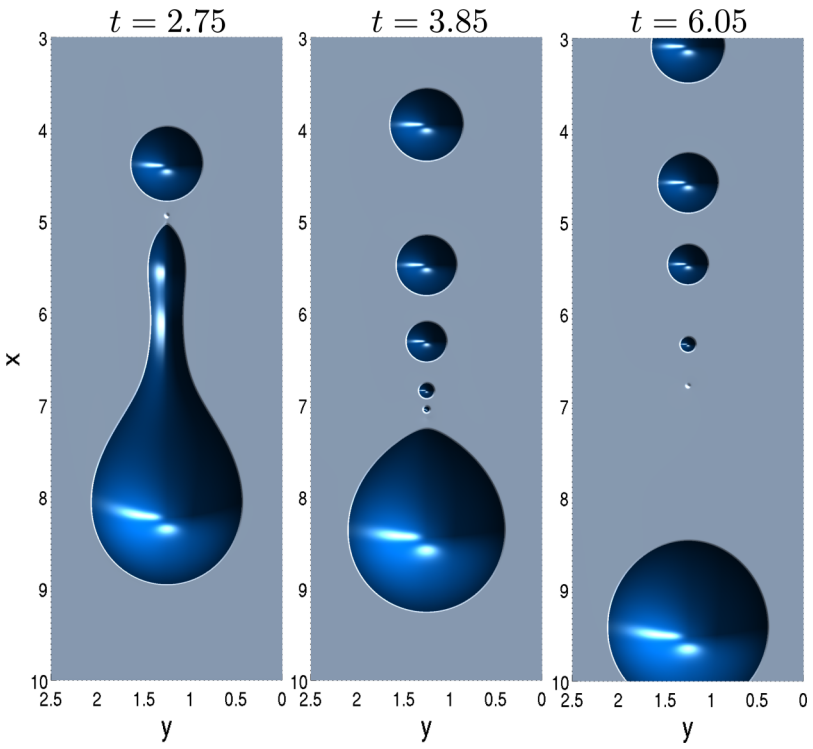

FIG. 10. Upward movement of pearls driven by opposing external shear on an 18 μL droplet moving down a vertical substrate ($\alpha = 90^\circ$). The parameters used in these simulations are the same as those in Fig. 9, but external shear is started impulsively at a later time, $t = 2.75$. All quantities shown are dimensionless. The image at time $t = 6.05$ was truncated to facilitate comparison with results at previous times.

droplet of Fig. 9 and the leading droplet of Fig. 10. Both droplets attain a terminal shape after a brief interval due to the interaction with the external shear. Since pearling does not occur for the droplet of Fig. 9, it has more mass, a larger maximum height, and thus a larger advancing contact angle than the terminal leading droplet of Fig. 10.

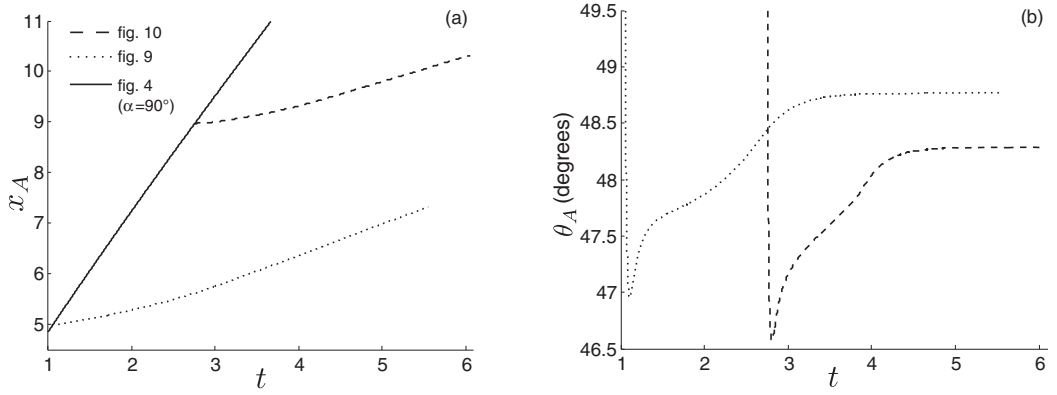

FIG. 11. (a) Positions of the apparent advancing contact lines vs time of the droplet of Fig. 9, and the leading droplets of Figs. 10 and 4 ($\alpha = 90^\circ$ case). (b) Apparent advancing contact angles vs time of the droplet of Fig. 9 and the leading droplet of Fig. 10. All quantities shown are dimensionless.

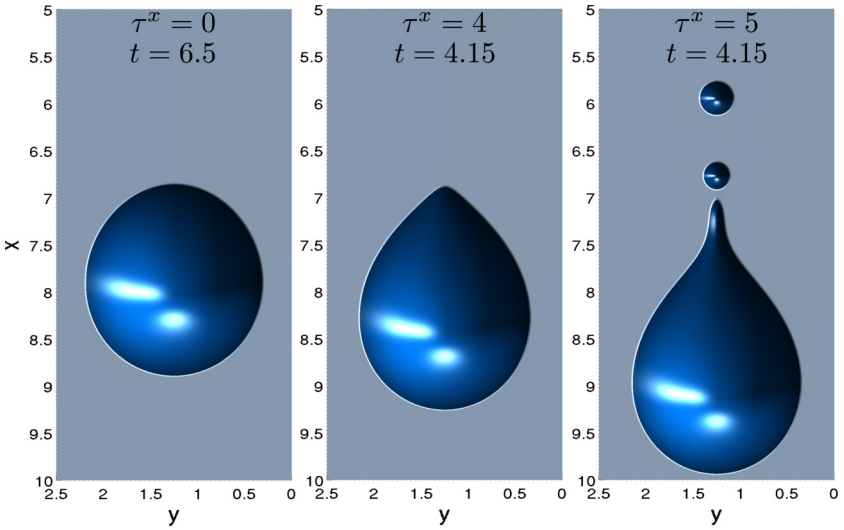

FIG. 12. Wetting transitions driven by external shear in the direction of droplet motion for 18 μL droplets on a substrate with inclination angle $\alpha = 26.3^\circ$. The parameters used in these simulations are $V_0 = 1.66$, $G_p = 4.16$, $G_n = 3.49$, $\tau^y = 0$, $\kappa = 0$, $\mathscr{A} = 7.29/b$ ($\theta_e = 45^\circ$), and $b = 5 \times 10^{-3}$. External shear is activated impulsively at time $t = 0.45$ in all the simulations. All quantities shown are dimensionless. The initial droplet shapes are the same as those used in Fig. 4.

C. External shear driving wetting transitions

We now discuss how external shear pushing a droplet in the direction of motion can force wetting transitions that would not be observed otherwise. To illustrate this, we focus on the 18 μL droplet moving on a substrate inclined at an angle $\alpha = 26.3^\circ$. As noted in Sec. IV A, under these conditions the droplet exhibits a round footprint when external shear is absent.

In Fig. 12, we show droplet shapes for different values of the external shear τ^x at given times. When $\tau^x = 0$, the terminal shape of the droplet has a round footprint (cf. Figs. 4 and 5) and the terminal speed is 5.2 cm/s. By forcing the droplet to move faster, external shear drives wetting transitions similar to those driven by gravitational forces (cf. Sec. IV). When $\tau^x = 4$, the droplet has a teardrop shape with terminal speed 9.0 cm/s. When $\tau^x = 5$, pearling is observed, and the terminal speed of the leading droplet is 9.9 cm/s.

The time evolution of the apparent advancing contact lines x_A of the droplets of Fig. 12 is shown in Fig. 13(a). This panel shows that all the droplets (leading droplet in the case $\tau^x = 5$) are traveling at terminal speeds. The corresponding time evolution of the apparent advancing contact angle θ_A for the cases $\tau^x = 4$ and 5 is shown in Fig. 13(b). For $\tau^x = 4$, where a teardrop shape is observed, the advancing contact angle reaches a terminal value. For $\tau^x = 5$, where pearling occurs, the leading droplet experiences a continuous decrease in height due to loss of mass. As a consequence, the advancing contact angle continues to decrease as time progresses. Similar behavior is seen in Fig. 5(c) as the inclination angle is varied in the absence of external shear.

In the absence of external shear, the onset of the teardrop shape can be understood by recognizing that there is a critical speed for liquid entrainment [1,31]. As the terminal speed of the droplet increases (via an increase in the inclination angle), apparent corners form so that the magnitude of the velocity normal to the contact does not exceed this critical value [1]. As the droplet speed increases further, the corners become more pronounced and a liquid neck forms. Eventually a steady state can no longer be sustained, and pearling occurs via a Plateau-Rayleigh mechanism.

In the presence of external shear, it appears that the terminal droplet speeds at which these transitions take place are not significantly affected. To illustrate this, we consider the terminal speed

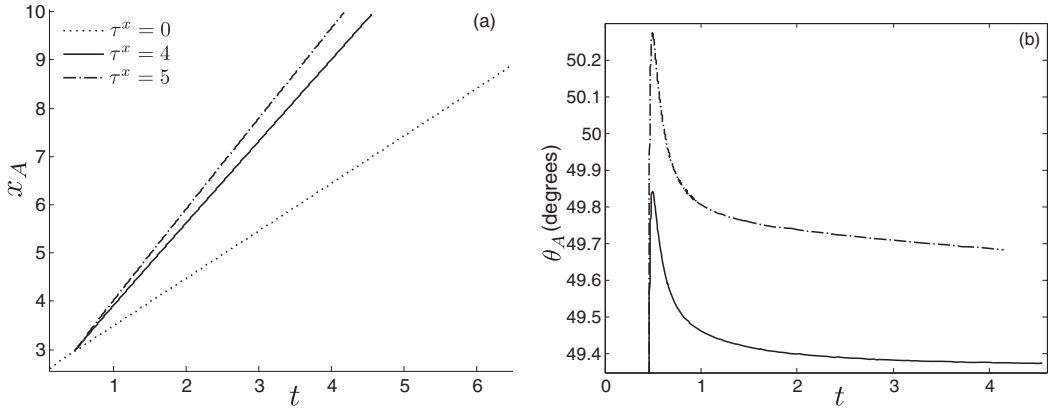

FIG. 13. (a) Positions of the apparent advancing contact lines vs time of the droplets of Fig. 12. (b) Apparent advancing contact angles vs time corresponding to the cases $\tau^x = 4$ and 5 of panel (a). For $\tau^x = 5$, the data in both panels correspond to the leading droplet. All quantities shown are dimensionless.

at which pearling first occurs. In the absence of external shear, pearling first occurs for the 18 μL droplet when the inclination angle is $\alpha \approx 55^\circ$, and the corresponding droplet speed is approximately 9.7 cm/s. When the inclination angle is reduced to $\alpha = 26.3^\circ$, pearling first occurs when when the external shear is $\tau^x \approx 5$ (Fig. 12). The corresponding droplet speed is approximately 9.9 cm/s, which is comparable to the value in the absence of external shear.

In Fig. 14, we show droplet shapes for both cases at the times when the first liquid pearl has been shed. Although there are pronounced differences in droplet shape, the speeds of the leading droplets are approximately the same (9.9 versus 9.7 cm/s). This suggests that even though each droplet is subject to different forces, the physical mechanisms governing the onset of pearling are very similar in the absence and presence of external shear.

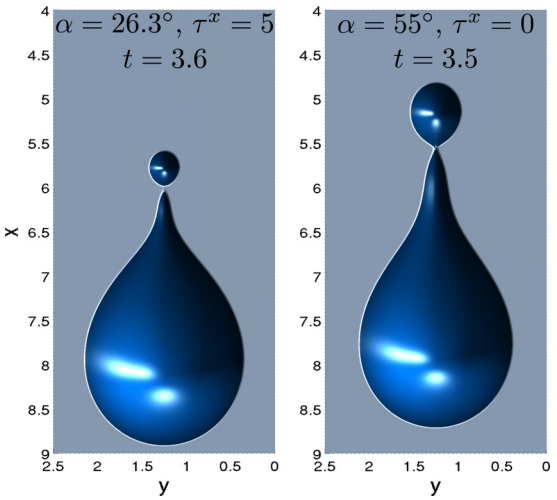

FIG. 14. Shapes of 18 μL droplets at the onset of pearling in the presence (left) and absence (right) of external shear. The parameters used in these simulations are $V_0 = 1.66$, $\tau^y = 0$, $\kappa = 0$, $\mathscr{A} = 7.29/b$ ($\theta_e = 45^\circ$), and $b = 5 \times 10^{-3}$. For the left image, $G_p = 4.16$ and $G_n = 3.49$, and for the right image, $G_p = 7.70$ and $G_n = 2.23$. External shear is activated impulsively at time $t = 0.45$. All quantities shown are dimensionless. The initial droplet shapes are the same as those used in Fig. 4.

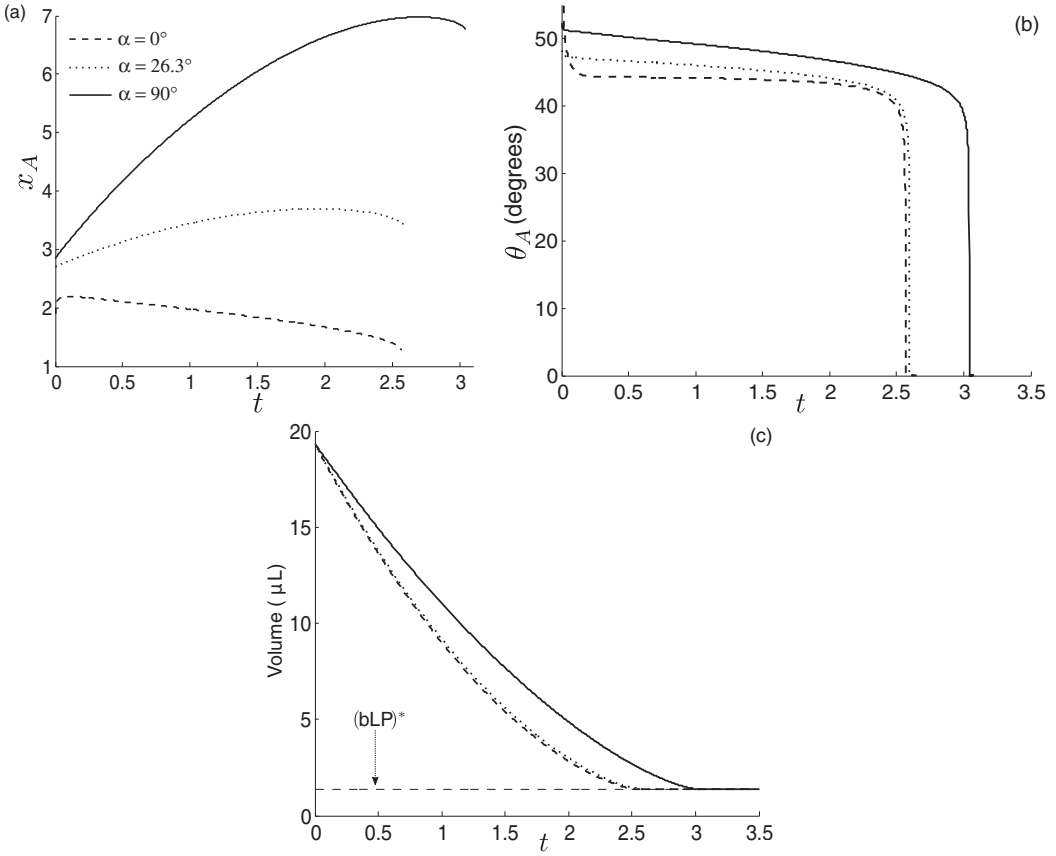

FIG. 15. Time evolution of (a) apparent advancing contact lines, (b) apparent advancing contact angles, and (c) volumes of 18 μL droplets moving on permeable substrates with inclination angle α with respect to the horizontal. All quantities shown are dimensionless, with the exception of the volume, which is shown in microliters. The quantity $(bLP)^*$ in panel (c) represents the volume of the precursor film. Except for the permeability $\kappa = 0.0498$, the parameters used in these simulations are the same as those in Fig. 4 ($G_n = 3.89$ and $G_p = 0$ when $\alpha = 0^\circ$).

VI. WETTING TRANSITIONS ON PERMEABLE SUBSTRATES

In this section, we investigate how substrate permeability affects droplet motion and wetting transitions. An immediate consequence of substrate permeability is the absence of steady states given that liquid absorption causes droplets to continuously lose mass, thereby altering droplet shape and motion.

To illustrate the effects of substrate permeability, we consider silicone oil droplets that have an initial volume of 18 μL. We take the dimensional permeability to be $\kappa^* = 4.55 \times 10^{-6}$ cm^2 and the substrate thickness to be $d^* = 0.13$ mm, which are within the range of values for silicone oil droplets spreading on fiber mats and membranes [11,32]. The equilibrium contact angle and precursor-film thickness are the same as those in previous sections.

In Fig. 15, we show the time evolution of the (a) apparent advancing contact lines, (b) apparent advancing contact angles, and (c) droplet volumes at several different inclination angles in the absence of external shear. As initial conditions for the nonzero inclination angles, we used solutions from simulations shown in Figs. 4 and 5 at times when the droplets were close to their terminal shapes. This significantly reduces computation times since it allows us to avoid simulating the

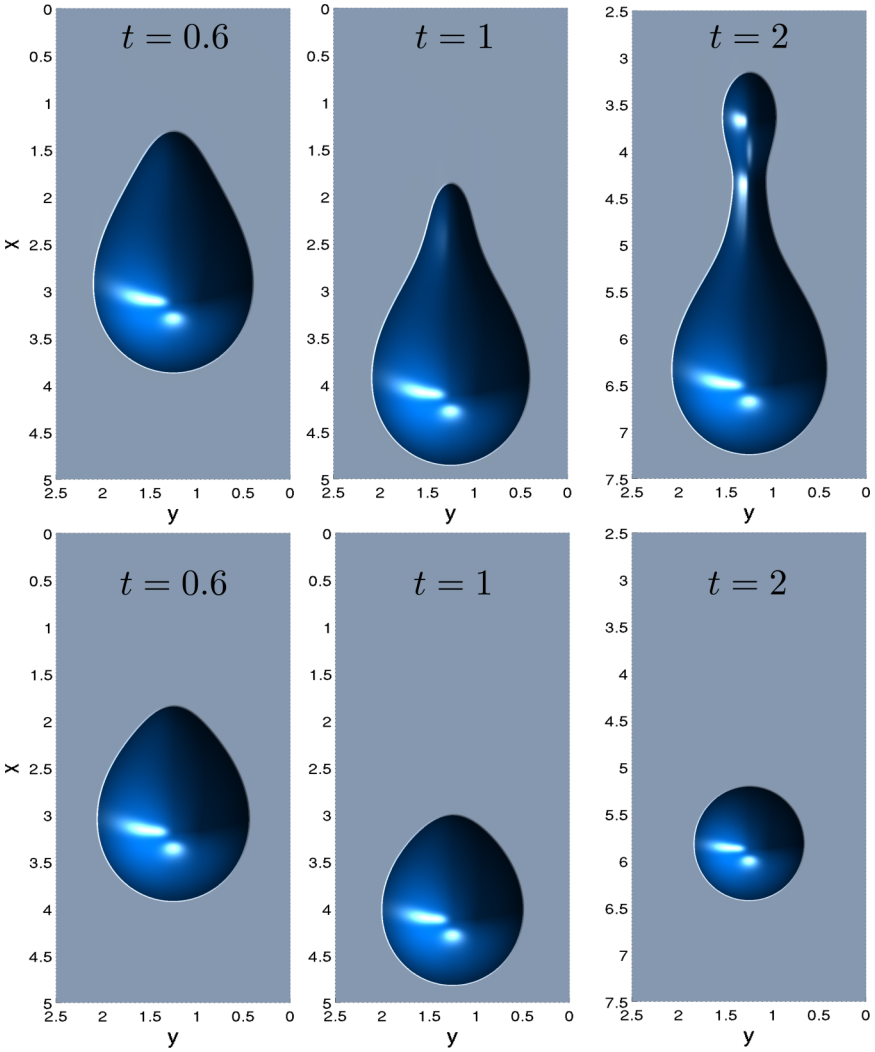

FIG. 16. Time evolution of 18 μL droplets moving down impermeable (first row) and permeable (second row) vertical substrates ($\alpha = 90^\circ$). The substrate permeability for the first row is $\kappa = 0$, and for the second row it is $\kappa = 0.0498$. All other parameters used in these simulations are the same as those in Fig. 4. All quantities shown are dimensionless.

earliest stages of droplet motion where the droplet rapidly relaxes from its initial condition. This choice of initial condition is reflected in Fig. 15(a), where the initial value of x_A increases with the inclination angle. Based on some limited runs we have performed, we note that the qualitative behavior of the results presented in this section is not affected by this choice of initial condition.

The behavior of the droplet on a horizontal permeable substrate ($\alpha = 0^\circ$) is consistent with what has been reported previously for axisymmetric droplets [11,32] (see also the Appendix). There is a short spreading period that occurs while the droplet surface relaxes to a spherical-cap shape characterized by the equilibrium contact angle θ_e [see the dashed curves in Figs. 15(a) and 15(b)]. This is immediately followed by a long retraction period due to liquid absorption by the substrate, during which the apparent contact angle remains close to θ_e [11]. The volume of the droplet decreases steadily until it reaches that of the precursor film on the rectangular domain of size $L \times P$ [dashed curve of Fig. 15(c)].

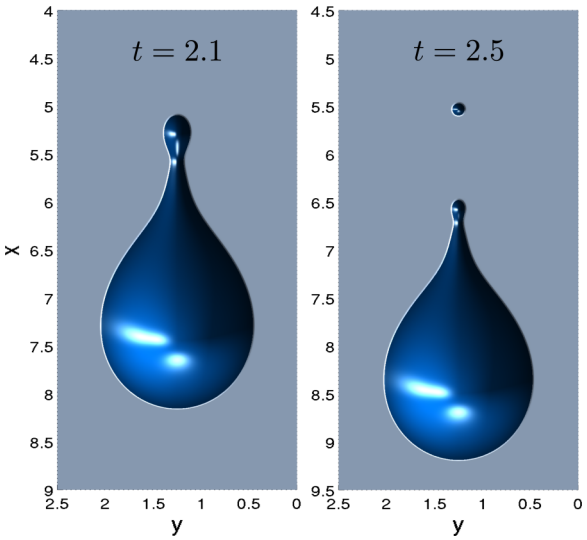

FIG. 17. Time evolution of an 18 μL droplet moving down a permeable substrate with an inclination angle $\alpha = 26.3^\circ$ and aided by external shear. The parameters used in these simulations are $V_0 = 1.66$, $G_p = 4.16$, $G_n = 3.49$, $\tau^x = 10$, $\tau^y = 0$, $\kappa = 0.01$, $\mathscr{A} = 7.29/b$ ($\theta_e = 45^\circ$), and $b = 5 \times 10^{-3}$. All quantities shown are dimensionless.

In contrast to the horizontal case, droplets on inclined permeable substrates display a much longer spreading period followed by a brief retraction [Fig. 15(a)]. Substrate inclination forces the droplets to tilt forward, increasing the droplet height with respect to the horizontal case, and as a consequence also the advancing contact angle [Fig. 15(b)]. However, as time progresses, this height difference is reduced because of the loss of liquid mass, which is reflected in the behavior of the advancing contact angle as well. The rate of liquid absorption decreases and the absorption time increases with substrate inclination angle [Fig. 15(c)]. This can be understood by recognizing that the hydrostatic component of the pressure decreases with increasing inclination angle, which reduces the driving force for liquid absorption.

The most interesting consequence of substrate permeability is that it tends to suppress the wetting transitions discussed in Sec. IV. We illustrate this in Fig. 16, where we compare the time evolution of droplets moving on impermeable (first row) and permeable (second row) vertical substrates. The first row of Fig. 16 shows the evolution of the droplet corresponding to the $\alpha = 90^\circ$ case of Fig. 4, close to the time when the first liquid pearl forms.

The second row of Fig. 16 shows how the droplet of the first row behaves when the substrate is permeable (the corresponding time evolution of various quantities characterizing this droplet is shown with continuous lines in Fig. 15). The steady loss of mass due to liquid absorption is evident in these images, and at $t = 2$, when enough liquid has been absorbed by the substrate, the droplet has reverted back to having a round footprint. It is also clear that liquid absorption has suppressed the formation of the long neck at the back of the droplet, which marks the start of the pearling process. This happens because liquid absorption increases with increasing capillary pressure, which is large in the region where the liquid neck is forming due to the large surface curvature.

However, droplet pearling can still be observed if the time scale associated with liquid absorption is small enough or the droplet speed is fast enough, as shown in Fig. 17. Here, droplet motion is aided by external shear, and the substrate permeability is smaller compared to the simulations of Figs. 15 and 16. Under these conditions, a liquid neck has time to form and stretch before it is absorbed.

Nevertheless, it is important to recognize that droplet wetting transitions are fundamentally altered by substrate permeability. For example, although teardrop shapes are observed on permeable

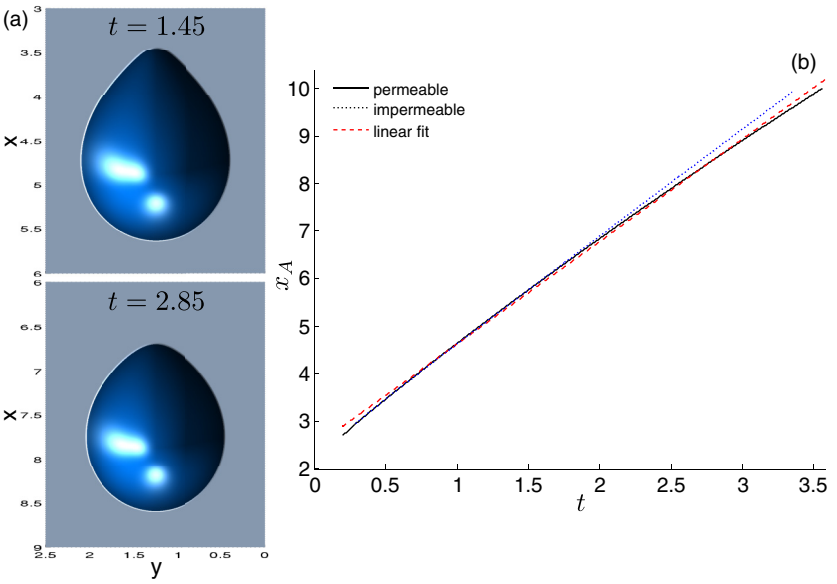

FIG. 18. (a) Time evolution of an 18 μL droplet moving down a permeable substrate with an inclination angle $\alpha = 26.3^\circ$ and aided by external shear $\tau^x = 7$. (b) Time evolution of the apparent advancing contact line of the droplet of (a). The red dashed line is a linear fit to the continuous curve, and the dotted line shows x_A when the substrate is impermeable ($\kappa = 0$). All other parameters used in these simulations are the same as those in Fig. 17. All quantities shown are dimensionless.

substrates (droplet of the second row of Fig. 16 at $t = 0.6$), they occur as transient states instead of the terminal shapes observed on impermeable substrates.

To further illustrate these differences, we consider the terminal droplet speed at which pearling first occurs. Recall from Sec. V C that for impermeable substrates, this speed was not significantly affected by external shear. However, this is no longer the case when the substrate is permeable.

To show this, we repeated the simulation of Fig. 17 with a smaller external-shear parameter ($\tau^x = 7$). Figure 18(a) shows that pearling does not occur (compare the time labels with those of Fig. 17), and Fig. 18(b) shows the time evolution of the apparent advancing contact line. Note that over the time interval shown, the droplet on the permeable substrate attains an approximately constant speed. A linear fit to the contact-line position allows us to estimate the droplet speed as 11.5 cm/s. The corresponding time evolution for a droplet on an impermeable substrate is also shown. Here, pearling occurs (images not shown), and the terminal speed of the leading droplet is 11.9 cm/s.

On an impermeable substrate, the critical terminal speed at which pearling first occurs in the absence of external shear is approximately 9.7 cm/s (Sec. V C and Fig. 14). The droplet of Fig. 18(b) on an impermeable substrate has a speed of 11.9 cm/s, which is larger than this critical speed, and pearling is indeed observed. However, the droplet of Fig. 18(b) on a permeable substrate has a speed (11.5 cm/s) that is also larger than this critical value, but pearling is not observed. This indicates that over the time interval considered, the effects of substrate permeability on droplet speed are relatively small, yet permeability has suppressed pearling.

VII. CONCLUSIONS

The results presented in this work show that external shear and substrate permeability have a significant influence on droplet wetting transitions on inclined substrates. If strong enough, external shear can balance the gravity-driven motion of a droplet, causing it to remain stationary or move

upward (Sec. V A). Remarkably, if the droplet is forced to remain stationary, it attains a shape that is close to what is observed for a droplet on a horizontal substrate. External shear inhibits the formation of a liquid neck at the rear of the droplet, and if applied early enough, it can stop the pearling process (Sec. V B). If pearls do form, external shear moves them upward while the leading droplet continues to move down the substrate. External shear can also drive wetting transitions similar to those driven by gravity (Sec. V C). It appears that the critical terminal droplet speeds at which these transitions occur are not significantly affected by external shear, suggesting that the physical mechanisms governing the onset of pearling are very similar in the presence and absence of external shear.

Substrate permeability leads to the absence of steady states because droplets continually lose mass (Sec. VI). As a consequence of this mass loss, pearling can be suppressed. If the droplet speed is sufficiently large (due to a low permeability or external shear), pearling can still occur. When it does, it appears that the critical droplet speed associated with the onset of pearling is significantly affected by substrate permeability. The strong influence of substrate permeability and external shear on droplet wetting transitions indicates that it will be important to account for these effects when developing accurate models for spray coating and filtration (Sec. I).

We close by highlighting several areas of future research suggested by our work. First, there is a need for systematic experiments to verify the theoretical predictions of this paper. Second, even for impermeable substrates, it would be useful to perform simulations of the full Stokes or Navier-Stokes equations with a Navier-slip boundary condition. This would enable the study of nonwetting droplets, which are beyond the reach of lubrication theory, and it would also allow one to overcome the limitations of using a precursor-film model (Sec. IV). Such simulations may also help to resolve the puzzling observation that unphysically small slip lengths are needed in various asymptotic theories for their predictions to match experimental observations [29,33]. Third, it will likely be important to account for contact angle hysteresis in the model to describe experimental observations, especially for the applications described in Sec. I, where substrate roughness is expected to be significant. This could be done by explicitly accounting for substrate topography and chemical heterogeneities (e.g., [34]). Finally, our results from Sec. VI suggest the need for a systematic study of wetting transitions on permeable substrates, similar to what has been accomplished for impermeable substrates [35–38].

ACKNOWLEDGMENTS

We thank Cummins Filtration for financial support of this work and for helpful discussions. We are grateful to the Minnesota Supercomputing Institute (MSI) at the University of Minnesota for providing computational resources.

APPENDIX: CODE VALIDATION

In this Appendix, we describe a couple of test cases used to validate our code. The first concerns a perfectly wetting droplet moving on a horizontal substrate in the presence of external shear. By assuming that the droplet is one-dimensional [$h = h(x,t)$], neglecting surface tension, and using arguments similar to those in Ref. [5], a self-similar solution can be derived:

$$h(x,t) = \frac{x}{\tau^x t}. \tag{A1}$$

Figure 19(a) shows that away from the droplet front, there is excellent agreement between the results from our simulation taken at the symmetry plane (at a given time) and the prediction of Eq. (A1). It is notable that even though the droplet in our simulation is two-dimensional (i.e., it has a finite extent in the y direction), the height profile at the symmetry plane matches that predicted by the self-similar solution, which is for one-dimensional droplets.

Figure 19(b) shows cross sections of the droplet from our simulations at different values of x. At the rear of the droplet, and close to the symmetry plane ($y = 1$), the rate of change of surface curvature with respect to x and y is relatively small, so surface-tension effects are not significant, which explains

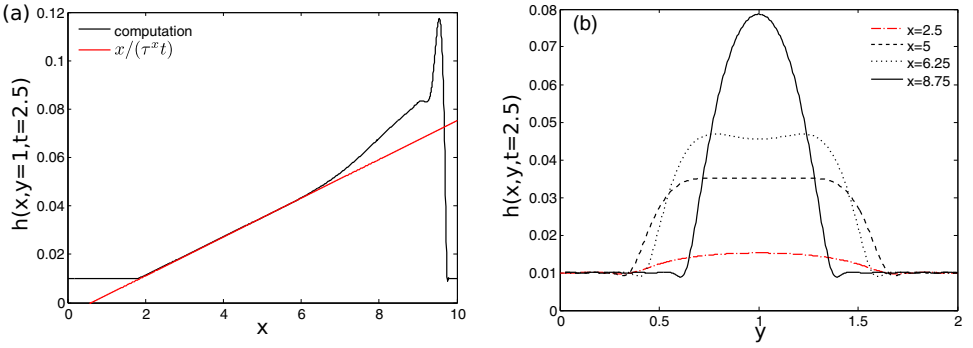

FIG. 19. (a) Droplet height profile at symmetry plane ($y = 1$) at $t = 2.5$ compared to prediction of Eq. (A1) (straight line). (b) Cross sections of droplet at different values of x. The parameters used in the simulations are $V_0 = 1$, $\kappa = 0$, $G_n = 0$, $G_p = 0$, $\tau^x = 50$, $\tau^y = 0$, $\mathscr{A} = 0$, and $b = 10^{-2}$. The initial condition was centered at $(x_0, y_0) = (1,1)$ with $r_0 = 0.25$.

the agreement with the self-similar solution shown in Fig. 19(a). However, when $x \gtrsim 6$, the rate of change of surface curvature becomes significant and surface tension can no longer be neglected.

The second test case concerns a droplet spreading on a horizontal permeable substrate in the absence of external shear. The axisymmetric version of this problem was considered in Ref. [11]. The results produced by the present code can be compared to the results of Ref. [11] by recognizing that if we start with an axisymmetric initial condition, the solution should remain axisymmetric in the absence of external shear.

In Fig. 20, we show a comparison of the results produced by the axisymmetric code [11] and the present code, which solves the full two-dimensional (2D) equations. For these simulations, we did not enforce any symmetry conditions, including at $y = y_0$. A droplet contact angle and contact-line position were extracted from the 2D simulations using the method described in Sec. III. The droplet radius is then taken to be $x_A - x_0$.

Figure 20(a) shows the time evolution of the droplet radius. The droplet initially spreads, and then a retraction period caused by liquid absorption into the substrate follows. Figure 20(b) shows that the apparent contact angle of the droplet decreases during spreading, and then remains close to

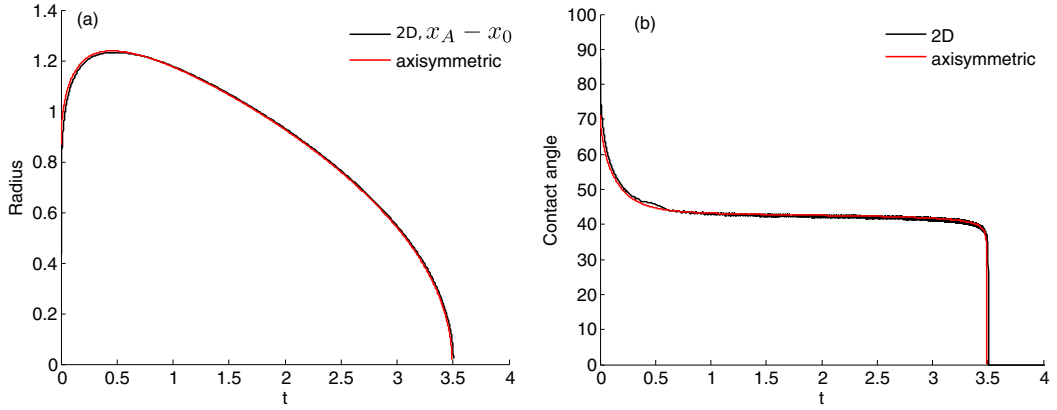

FIG. 20. Time evolution of (a) radius and (b) apparent contact angle for a droplet spreading on a horizontal, permeable substrate. The parameters used in our simulations are $V_0 = 2$, $G_p = G_n = 0$, $\tau^x = \tau^y = 0$, $\kappa = 0.1$, $\mathscr{A} = 1/b$ ($\theta_e = 43.31°$), and $b = 10^{-3}$. The initial condition was centered at $(x_0 = 1, y_0 = 1)$ with $r_0 = 0.5$. The red curves (axisymmetric) are from Fig. 5 of Espín and Kumar [11].

its equilibrium value during retraction [11]. When the origin of the coordinate system for the 2D simulations is translated to (x_0, y_0), it is seen that the results from those simulations are in excellent agreement with those obtained using the axisymmetric code.

[1] T. Podgorski, J. M. Flesselles, and L. Limat, Corners, Cusps, and Pearls in Running Drops, Phys. Rev. Lett. **87**, 036102 (2001).

[2] N. Le Grand, A. Daerr, and L. Limat, Shape and motion of drops sliding down an inclined plane, J. Fluid Mech. **541**, 293 (2005).

[3] L. W. Schwartz, D. Roux, and J. J. Cooper-White, On the shapes of droplets that are sliding on a vertical wall, Physica D **209**, 236 (2005).

[4] G. Ahmed, M. Sellier, M. Jermy, and M. Taylor, Modeling the effects of contact angle hysteresis on the sliding of droplets down inclined surfaces, Eur. J. Mech. B-Fluids **48**, 218 (2014).

[5] J. A. Moriarty, L. W. Schwartz, and E. O. Tuck, Unsteady spreading of thin liquid films with small surface tension, Phys. Fluids **3**, 733 (1991).

[6] I. S. McKinley, S. K. Wilson, and B. R. Duffy, Spin coating and air-jet blowing of thin viscous drops, Phys. Fluids **11**, 30 (1999).

[7] P. Dimitrakopoulos, Deformation of a droplet adhering to a solid surface in shear flow: Onset of interfacial sliding, J. Fluid Mech. **580**, 451 (2007).

[8] P. Dimitrakopoulos, Gravitational effects on the deformation of a droplet adhering to a horizontal solid surface in shear flow, Phys. Fluids **19**, 122105 (2007).

[9] J. Fan, M. C. T. Wilson, and N. Kapur, Displacement of liquid droplets on a surface by a shearing air flow, J. Colloid Interface Sci. **356**, 286 (2011).

[10] A. Hashimoto, M. Sakai, J.-H. Song, N. Yoshida, S. Suzuki, Y. Kameshima, and A. Nakajima, Direct observation of water droplet motion on a hydrophobic self-assembled monolayer surface under airflow, J. Surf. Finish. Soc. Jpn. **59**, 907 (2008).

[11] L. Espín and S. Kumar, Droplet spreading and absorption on rough, permeable substrates, J. Fluid Mech. **784**, 465 (2015).

[12] L. Espín and S. Kumar, Forced spreading of films and droplets of colloidal suspensions, J. Fluid Mech. **742**, 495 (2014).

[13] L. Espín and S. Kumar, Sagging of evaporating droplets of colloidal suspensions on inclined substrates, Langmuir **30**, 11966 (2014).

[14] Z. Wang, L. Espín, F. S. Bates, S. Kumar, and C. W. Macosko, Water droplet spreading and imbibition on superhydrophilic poly(butylene terephthalate) melt-blown fiber mats, Chem. Eng. Sci. **146**, 104 (2016).

[15] A. Oron, S. H. Davis, and S. G. Bankoff, Long-scale evolution of thin liquid films, Rev. Mod. Phys. **69**, 931 (1997).

[16] N. Alleborn and H. Raszillier, Spreading and sorption of a droplet on a porous substrate, Chem. Eng. Sci. **59**, 2071 (2004).

[17] R. V. Craster and O. K. Matar, Dynamics and stability of thin liquid films, Rev. Mod. Phys. **81**, 1131 (2009).

[18] T. P. Witelski and M. Bowen, ADI schemes for higher-order nonlinear diffusion equations, Appl. Numer. Math. **45**, 331 (2003).

[19] M. R. Mata and A. L. Bertozzi, A numerical scheme for particle-laden thin film flow in two dimensions, J. Comput. Phys. **230**, 6334 (2011).

[20] L. W. Schwartz, Hysteretic effects in droplet motions on heterogeneous substrates: Direct numerical simulation, Langmuir **14**, 3440 (1998).

[21] L. W. Schwartz and R. R. Eley, Simulation of droplet motion on low-energy and heterogeneous surfaces, J. Colloid Interface Sci. **202**, 173 (1998).

[22] H.-Y. Kim, H. J. Lee, and B. H. Kang, Sliding of liquid drops down an inclined solid surface, J. Colloid Interface Sci. **247**, 372 (2002).

[23] R. Krechetnikov, On application of lubrication approximations to nonunidirectional coating flows with clean and surfactant interfaces, Phys. Fluids **22**, 092102 (2010).
[24] R. Tadmor, Line energy and the relation between advancing, receding, and young contact angles, Langmuir **20**, 7659 (2004).
[25] M. N. Popescu, G. Oshanin, S. Dietrich, and A-M. Cazabat, Precursor films in wetting phenomena, J. Phys. Condens. Matter **24**, 243102 (2012).
[26] Y. Y. Koh, Y. C. Lee, P. H. Gaskell, P. K. Jimack, and H. M. Thompson, Droplet migration: Quantitative comparisons with experiment, Eur. Phys. J.-Spec. Top. **166**, 117 (2009).
[27] L. W. Schwartz and S. Garoff, Contact angle hysteresis and the shape of the three-phase line, J. Colloid Interface Sci. **106**, 422 (1985).
[28] R. Golestanian and E. Raphaël, Roughening transition in a moving contact line, Phys. Rev. E **67**, 031603 (2003).
[29] E. S. Benilov and M. S. Benilov, A thin drop sliding down an inclined plate, J. Fluid Mech. **773**, 75 (2015).
[30] P. G. Simpkins and E. L. Bales, Water-drop response to sudden accelerations, J. Fluid Mech. **55**, 629 (1972).
[31] T. D. Blake and K. J. Ruschak, A maximum speed of wetting, Nature (London) **282**, 489 (1979).
[32] V. M. Starov, S. R. Kostvintsev, V. D. Sobolev, M. G. Velarde, and S. A. Zhdanov, Spreading of liquid drops over dry porous layers: Complete wetting case, J. Colloid Interface Sci. **252**, 397 (2002).
[33] B. A. Puthenveettil, V. K. Senthilkumar, and E. J. Hopfinger, Motions of droplets on inclined surfaces in the inertial regime, J. Fluid Mech. **726**, 26 (2013).
[34] N. Savva and S. Kalliadasis, Droplet motion on inclined heterogeneous substrates, J. Fluid Mech. **725**, 462 (2013).
[35] J. H. Snoeijer and B. Andreotti, Moving contact lines: Scales, regimes, and dynamical transitions, Annu. Rev. Fluid Mech. **45**, 269 (2013).
[36] E. Vandre, M. S. Carvalho, and S. Kumar, Delaying the onset of dynamic wetting failure through meniscus confinement, J. Fluid Mech. **707**, 496 (2012).
[37] E. Vandre, M. S. Carvalho, and S. Kumar, On the mechanism of wetting failure during fluid displacement along a moving substrate, Phys. Fluids **25**, 102103 (2013).
[38] E. Vandre, M. S. Carvalho, and S. Kumar, Characteristics of air entrainment during dynamic wetting failure along a planar substrate, J. Fluid Mech. **747**, 119 (2014).